EPR studies of defects in electron-irradiated silicon: A triplet state of vacancy-oxygen complexes*

Young-Hoon Lee and James W. Corbett
Department of Physics, State University of New York at Albany, Albany, New York 12222
(Received 25 March 1975)

Three new EPR spectra (Si-*A*14, -*A*15, and -*A*16) and two previously known spectra (Si-*P*2 and -*P*4) are observed for the first time in electron-irradiated silicon. The microscopic defect models are established as multivacancy-oxygen complexes with the oxygen(s) in Si-O-Si structure inside the ⟨110⟩ vacancy chain: a (divacancy plus oxygen) for Si-*A*14, a (divacancy plus two oxygen) for Si-*P*2, a (trivacancy plus oxygen) for Si-*P*4, a (trivacancy plus two oxygen) for Si-*P*5, and a (trivacancy plus three oxygen) for Si-*A*15. The number of vacancies in the ⟨110⟩ chain is determined from the zero-field fine structure and the number of oxygens from the evolutionary kinetics, with the *g* tensor, ^{29}Si hyperfine structure, and stress response providing strong supportive evidence. It is emphasized that some of these oxygen-dependent defects play an important role as trapping centers for other point defects.

I. INTRODUCTION

Electron paramagnetic resonance of radiation-induced defects has been extensively studied for[1,2] electron- and[3–5] neutron-irradiated silicon. Approximately sixty spectra have been identified, with approximately twenty cases having a clear identification of the microscopic defect structure. It is also generally accepted from the known defects in silicon that low-energy-electron damage produces simple defects such as the vacancy, divacancy, and vacancy-impurity pair. Neutrons create larger, complex defects such as tetra- or penta-vacancy centers, in addition to those defects found in the electron bombardment. However, it is not clearly understood what happens after the divacancy center disappears at 350 °C, since no spectrum has been observed above that temperature in electron-irradiated silicon.

The present work was initiated to understand the intermediate situation between the low-energy-electron- and the neutron-radiation damage. A similar study was reported by Daly and Noffke[6] who used a low-fluence neutron bombardment ($\sim 10^{15}$ neutrons/cm^2) to observe a number of the spectra dominant in electron-irradiated silicon, as well as those in neutron-irradiated silicon. We used 2-MeV electrons to see whether a high-fluence (10^{18}–10^{19} electrons/cm^2) produces those spectra previously found in neutron-irradiated silicon. In Czochralski grown silicon, we not only observed the oxygen-dependent spin-1 centers which have been only found in neutron-bombarded silicon, but resolved three new, oxygen-dependent spectra. We constructed defect models for the oxygen-dependent spin-1 centers in terms of oxygen-multivacancy complexes. We will argue that the following sequence of anneal recovery stages takes place in pulled silicon: (i) the divacancy $[V_2]$, (vacancy + oxygen) $[V+O]$, and (divacancy + oxygen) $[V_2+O]$ (Si-*A*14),[7] centers are equally probable below 350 °C; (ii) these three centers disappear at 350 °C yielding the (divacancy + 2 oxygen) $[V_2+O_2]$ (*P*2) and (trivacancy + oxygen) $[V_3+O]$ (*P*4) centers; (iii) these latter centers disappear at 400 °C yielding the (trivacancy + 2 oxygen) $[V_3+O_2]$ (*P*5) and (trivacancy + 3 oxygen) $[V_3+O_3]$ (*A*15) centers. Thus, the following families of defects now can be identified:

(i) Intrinsic vacancy (*V*)-type defects: $[V^+]$,[8–11] $[V_2^{\pm}]$,[12–16] $[V_3]$,[17,18] $[V_4$ (planar)],[19] $[V_4$ (non-planar)],[17,18] and $[V_5]$[4];

(ii) (nearly-substitutional oxygen plus vacancy)-type defects: $[(V+O)^{\pm,0}]$,[20–25] $[(V+O)^*]$,[26] $[V_2+O]$,[27] $[V_2+O_2]$,[27] $[V_3+O]$,[19,27] $[V_3+O_2]$,[27] and $[V_3+O_3]$[27]; and

(iii) (substitutional impurity plus vacancy)-type defects: $[V+P]$,[1,9,28] $[V+As]$,[9,29,30] $[V+Sb]$,[9,29,30] $[V+B]$,[9,29] $[V+Al]$,[9,10,29,30] $[V+Ga]$,[29] $[V+C]$,[31–33] $[V+Ge]$,[11,34,35] and $[V+Sn]$.[35]

After a brief description of the experimental procedures in Sec. II, we present in Sec. III the new EPR coupling tensors for the Si-*P*2 and -*P*4 spectra as well as for three new spectra, Si-*A*14, -*A*15, and -*A*16. Section IV gives a discussion of the ^{29}Si hyperfine structure and the fine structure of the triplet state. Based on these data, we will establish defect models and electronic structures for the spin-1 centers. In Sec. V we describe supporting evidence for the models obtained from the ⟨110⟩-stress alignment of the spectra. Section VI is a summary.

II. EXPERIMENTAL PROCEDURE

Electron irradiation was performed at the 4-MeV Dynamitron at SUNY/Albany. The samples were cut from a single crystal boule along the ⟨110⟩ crystallographic axis with a cross section of 2 × 2 mm^2 and then irradiated at room temperature (sample temperature $\lesssim$100 °C) with 2.0-MeV elec-

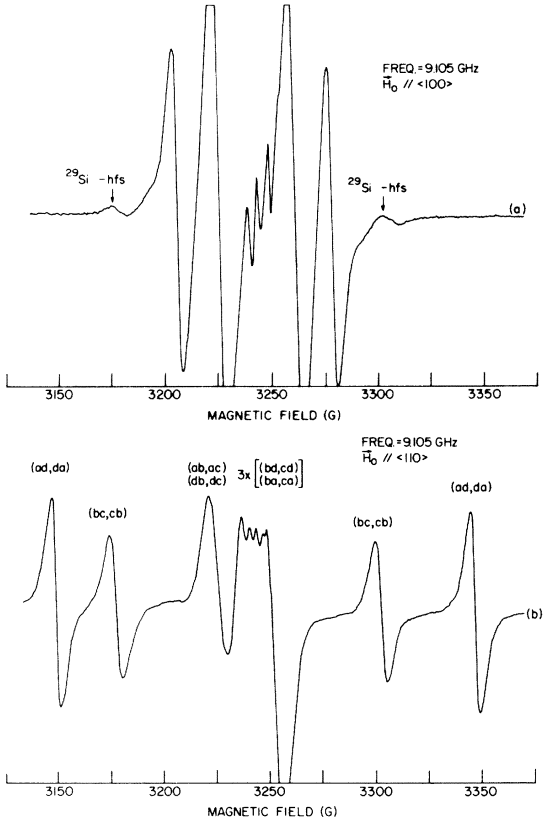

FIG. 1. Si-$A14$ (V_2+O] spectrum at 77 °K; (a) $\vec{H}_0$ ∥ ⟨100⟩ and (b) $\vec{H}_0$ ∥ ⟨110⟩. The ^{29}Si hyperfine satellites are indicated in (a) and each EPR signal is labeled by the corresponding defect site in (b).

trons. The total electron fluence ranged between 5.0×10^{17} and 1.2×10^{19} electrons/cm^2. This paper is mainly concerned with our experimental results obtained from n- and p-type Czochralski grown silicon, in which the oxygen concentration is estimated to be ~10^{18} atoms/cm^3 based on the 9.0-μm ir band. The initial resistivity prior to irradiation ranged between 1.0 and 10.0 Ω cm.

EPR measurements were made with 9.5- and 35-GHz Varian spectrometers and sample temperatures from 77–300 °K. The relative intensity of EPR spectra was measured with the Mn^{2+} EPR signal due to a known number of spins. The total intensity was measured from the fine-structure lines and their peak-to-peak linewidth, ignoring the intensity of the ^{29}Si hfs lines.

III. EXPERIMENTAL RESULTS

A. Si-$A14$ spectrum

Figure 1 shows the EPR signal taken at 77 °K with the external magnetic field $\vec{H}_0$ parallel to the ⟨100⟩ and ⟨110⟩ crystallographic axes; in Fig. 1(a), we also indicate the hyperfine satellites (hfs) due to the ^{29}Si isotope ($I=\frac{1}{2}$ and natural abundance 4.7%) in the vicinity of the defect. This new spectrum, named as $A14$, is observed only in Czochralski-grown silicon, and not in float-zone refined samples. Three weak lines near 3250 G could not be identified because of severe overlap at other angles. Beside this new spectrum, we resolved the known spectra, $B1$, $G7$, $G8$, $G15$, and $G16$ in various samples. We did not observe the $P3$, $P6$, and $A5$ spectra which were found in[3,17] neutron- and in[36,37] heavy-ion bombarded silicon.

The $A14$ spectrum requires the spin Hamiltonian

$$\mathcal{H}=\mu_B\vec{H}\cdot\overleftrightarrow{g}\cdot\vec{S}+\vec{S}\cdot\overleftrightarrow{D}\cdot\vec{S}+\sum_j\vec{I}_j\cdot\overleftrightarrow{A}_j\cdot\vec{S}\,, \qquad (1)$$

with the effective spin $S=1$ to describe the angular variation of the spectrum. The first term presents the electronic Zeeman interaction, the second term is the fine structure, and the last the magnetic hyperfine interaction with a nuclear spin I_j. The angular dependence is shown in Fig. 2(a), where the solid lines represent the fine-structure lines calculated from Eq. (1) using the coupling parameters in Table I and the coordinates shown in Fig. 3. The resolved hyperfine structure due to the ^{29}Si isotopes is given in Fig. 2(b); the intensity ratio of the hfs line to the corresponding central line is 5.3% indicating that two equivalent sites participate in the hyperfine interaction. The hyperfine axis ($A_{\|}$) is parallel to a ⟨111⟩ crystal axis. For later use, each fine-structure line in Figs. 1(b) and 2(a) is denoted by a corresponding defect site with respect to the laboratory system in Fig. 3; e.g., ad represents a defect whose g_1 axis is closest to $[11\bar{1}]$ (d) and g_3 axis closest to $[1\bar{1}1]$ (a) as shown in Fig. 3.

The total intensity of the $A14$ spectrum was measured at 77 °K as a function of the electron fluence, and the results are given in Fig. 4. The $A14$ defect grows linearly with the fluence and saturates at a fluence of approximately 8×10^{18} electron/cm^2, where the estimated spin density is 2×10^{17} spins/cm^3. The production rate is approximately 0.05 cm^{-1}. We note that the defect production rate of the $[V+O]$ center is 0.1 cm^{-1} at $E=2.0$ Mev and of the $[V_2]$ center is 0.01 cm^{-1} at the same energy.[16] This comparison suggests that the $A14$ defect is produced by a direct collision process and is a major defect.

The amplitude (peak-to-peak height, A_{pp}) of the ad site appears to be larger than that of the bc site, as shown in Fig. 1(b), but their intensities $[(\Delta H_{pp})^2\times A_{pp}]$ are identical to each other, as expected if the defects are equally populated among differently oriented sites. The peak-to-peak half-width (ΔH_{pp}) at 77 °K is 6.1 G at the bc site and 4.9 G at the ad site. The difference in the amplitude between these two defect sites is observed

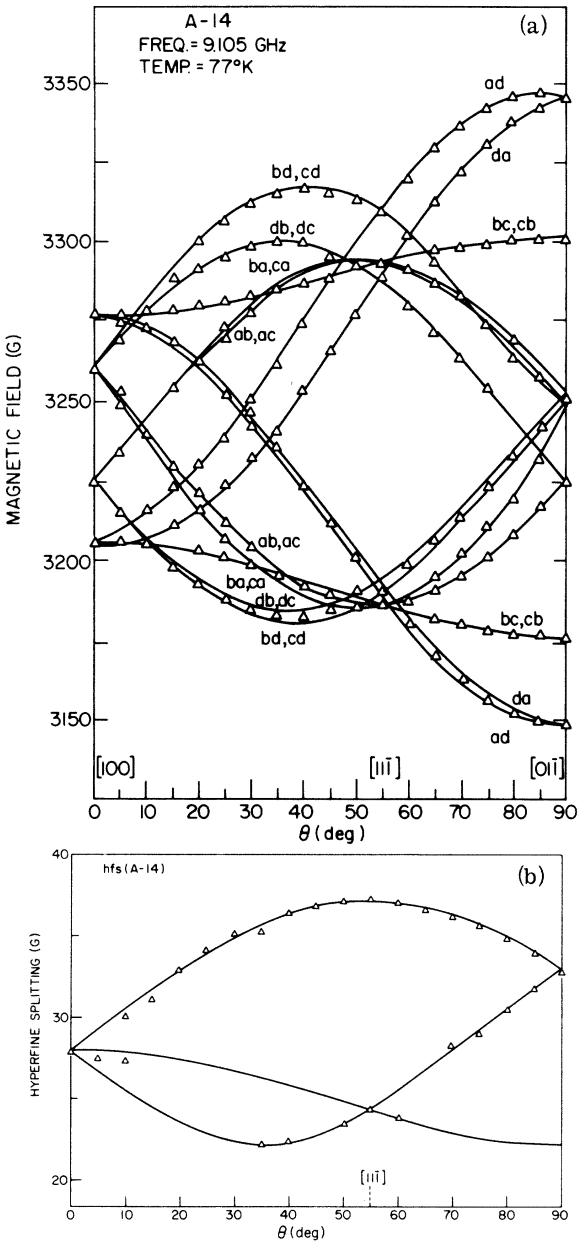

FIG. 2. Angular variation of the $A14$ $[V_2+O]$ spectrum in the $\{110\}$ plane at 77 °K; (a) the fine structure and (b) the hyperfine structure due to ^{29}Si. The solid lines are from theoretical calculation and the measurement was made at $\nu = 9.105$ GHz. Each fine structure line is labeled by the corresponding defect orientation in the lattice.

without regard to the bombarding electron beam direction, namely, either along a $\langle 110\rangle$ or $\langle 100\rangle$, and is persistent under heat treatment until the spectrum anneals (350 °C).

Two samples, n and p types of Czochralski grown silicon were heat treated in an argon ambient for 30 min and EPR measurements were performed at 77 °K with the 9.5 GHz bridge. Beyond 350 °C,

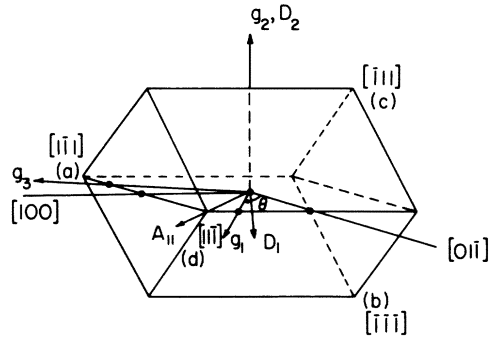

FIG. 3. Geometry and axes of the principal coordinates.

only the p-type sample was studied in detail. The results are shown in Fig. 5. Heat treatment produces two new spectra, labeled as $A15$ and $A16$ and two spectra ($P2$ and $P4$) known in neutron-irradiated silicon[3] (these four spectra are also oxygen dependent). We note that a similar annealing behavior was observed in neutron-irradiated silicon[3] in the temperature range 300–500 °C and that no spectrum has been previously observed at any temperature above 350 °C in electron-irradiated silicon.

B. Other information about the spectra

Figure 6 shows the EPR spectra taken with $\vec{H}_0 \parallel \langle 100\rangle$ in a p-type pulled silicon irradiated to 5×10^{18} electrons/cm^2: (a) after annealing at 350 °C and (b) after 450 °C annealing. The angular variation of the $A15$ spectrum in the $\{110\}$ plane is shown in Fig. 7; the solid lines are again theoretical predictions from Eq. (1) using the parameters in Table I determined by the least-squares method.[3] The $A15$ spectrum has a triplet spin state ($S=1$) as confirmed by the EPR data at two different frequencies, 9.1 and 35 GHz. The $A16$ spectrum re-

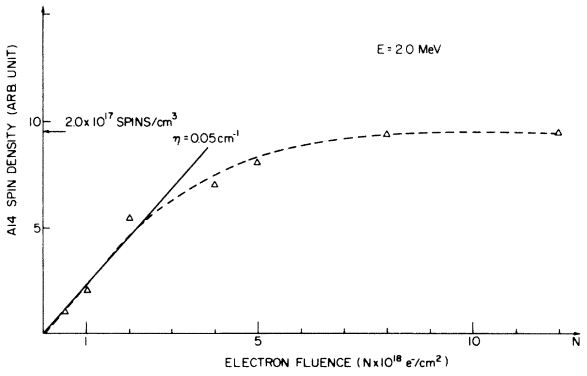

FIG. 4. Spin density of Si-$A14$ $[V_2+O]$ vs electron fluence. The measurement was made at 77 °K with the n-type sample ($\rho_0 = 1.0$ Ω cm). The rf power at the cavity was fixed at 4.0 mW. The production rate is estimated to be $\eta = 0.05$ cm^{-1} at $E = 2.0$ MeV.

TABLE I. Coupling parameters of EPR centers.

Spectrum[a]	g_1	g_2	g_3	θ_g	D_1 A_1	D_2 A_2	D_3 A_3	θ_D θ_A
Si-*A*14	2.0022	2.0088	2.0087	27.7°	∓61.8 69.5	±38.5 41.6	±21.6 41.6	7.0° 36°
Si-*A*15	2.0045	2.0115	2.0085	0°	∓35.3 ...	±18.1 ...	±17.4 ...	0° ...
Si-*A*16	2.0036	2.0112	2.0071	0°	... ...	... ...	... ...	... ...
Si-*P*2[b]	2.0019	2.0088	2.0099	32.0°	∓69.4 66.1	±39.7 37.0	±27.0 37.0	6.4° 36°
Si-*P*2[c]	2.0020	2.0088	2.0098	37.0°	∓68.7 ...	±39.6 ...	±29.1 ...	8.3° ...
Si-*P*4[b]	2.0036	2.0082	2.0066	−2.9°	∓27.5 65.7	±13.0 45.5	±14.4 45.5	6.5° ±36°
Si-*P*4[c]	2.0041	2.0089	2.0073	−6.9°	∓27.9 ...	±13.3 ...	±14.6 ...	6.2° ...
Si-*P*5[c]	2.0050	2.0091	2.0072	0.°	∓30.3 ...	±15.3 ...	±15.0 ...	0.° ...

[a]Error ranges are $\Delta g_i = \pm 0.0003$, $\Delta D_i = \pm 0.5 \times 10^{-4}$ cm^{-1}, and $\Delta\theta_g = \Delta\theta_D = \pm 1.0°$. *A*-16 is a spin = $\frac{1}{2}$ center; the rest are spin = 1. Both D_i and A_i values are in 10^{-4} cm^{-1}.

[b]Present data.

[c]Reference 3.

quires photoillumination to isolate its central lines from the fine-structure lines of other spectra and is found to be a spin-$\frac{1}{2}$ center with C_{2v} symmetry (see Table I).

The present determination of the EPR parameters for the oxygen-dependent spin-1 centers is given in Table I along with the previous one determined by Jung and Newell[3] at the same frequency (9.3 GHz). The *A*15 spectrum shows a large discrepancy from the *P*5 spectrum in the g and D tensors, although the symmetry axes are matched exactly and the annealing behaviors are identical. Particularly, the difference in the D_1 value is about 5 G which corresponds to 15 G in the actual separation between the fine-structure pair, far outside the error range; hence the identification as a new center. The present *P*2 and *P*4 data are essentially identical to the previous one within the error range. We presume that the difference in their g and D tensors is due to a slightly different environment of the defect. This difference could be due to the difference between electron and neutron bombardments, e.g., neutron irradiation produces various defect complexes[1] that are absent in the electron case, and neutrons are known to produce a heavily damaged core region.[38] We note, however, that the difference is not just the presence of a general strain, for in that case there would be a range of D parameters; instead the discrete difference between the spectra suggests a discrete difference in the centers such as might arise from the presence of a specific additional defect near one of the centers, as seems to occur with the "locked divacancies."[26]

In these experiments we were able to resolve, for the first time, ^{29}Si hyperfine structure of the *P*2 and *P*4 spectra. Figure 8(a) shows the angular dependence of the A tensor of the *P*2 spectrum, and the A-tensor variation of *P*4 is shown in Fig. 8(b). The relative intensity of the hfs line to the

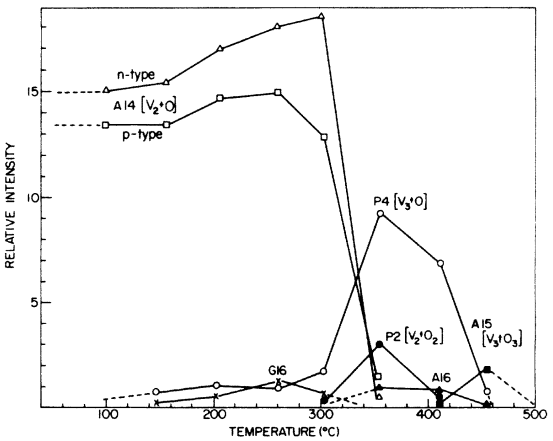

FIG. 5. Isochronal annealing (30 min) of a Czochralski-grown silicon after being irradiated with the 2.0-MeV electrons (fluence = 5.0×10^{18} electrons (cm^2).

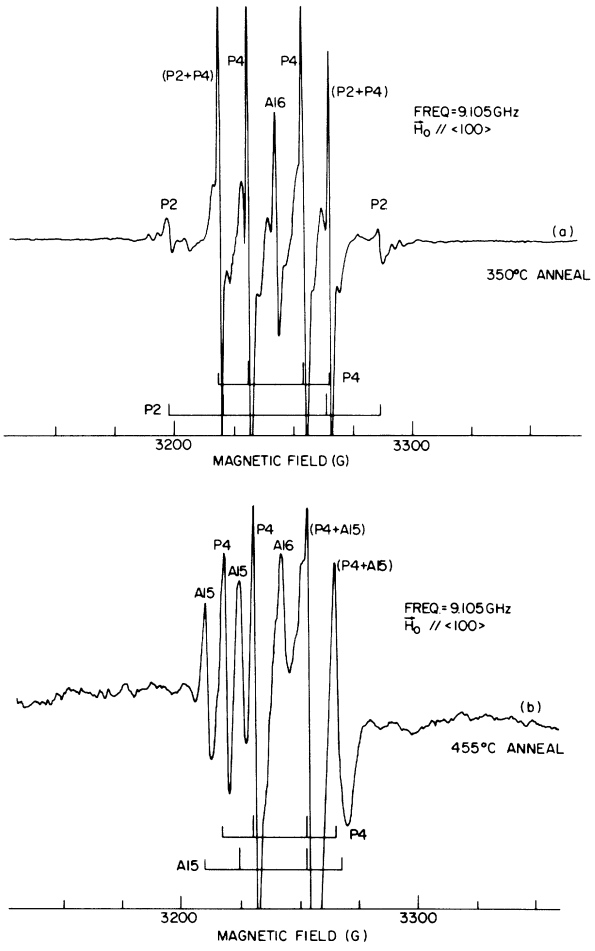

FIG. 6. Actual EPR signal at $\vec{H}_0 \parallel \langle 100 \rangle$; (a) after annealed at 350 °C and (b) at 455 °C. The relative intensity among the fine-structure lines are indicated in each spectrum.

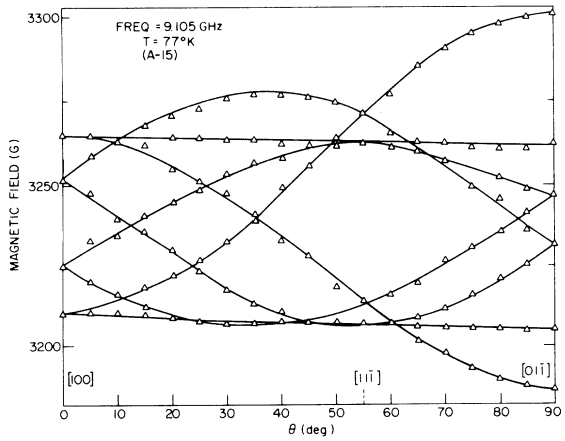

FIG. 7. Angular variation of the $A15$ $[V_3 + O_3]$ spectrum in the (110) plane.

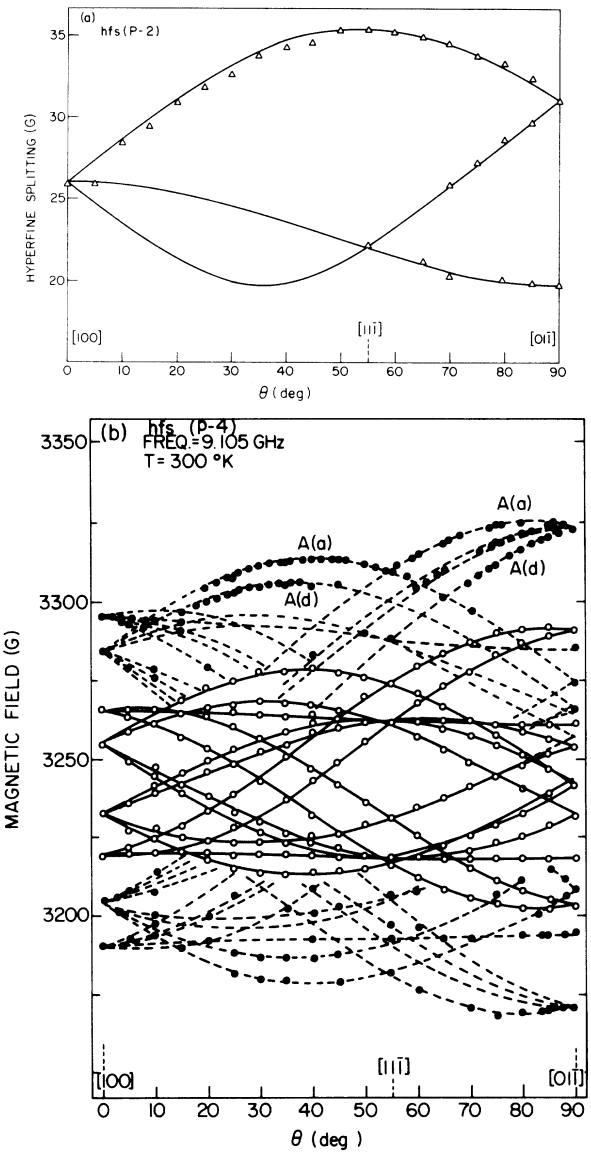

FIG. 8. Angular dependence of the ^{29}Si hyperfine structure: (a) the $P2$ $[V_2 + O_2]$ spectrum in the {110} plane; (b) the $P4$ $[V_3 + O]$ spectrum. In the $P4$ spectrum the solid lines (–o–) are the fine structure and the dashed lines (–●–) the ^{29}Si hyperfine structure; $A(a)$ and $A(d)$ in the hfs lines denote two distinct sets of the hfs structure (see the text for details).

central line is 5.2% for the $P2$ and 4.8% for $P4$, indicating that two nuclear sites are involved in the hfs interaction for both spectra. The hyperfine axis ($A_{\parallel}$) of $P2$ is parallel to a ⟨111⟩ axis. In $P4$, there are two different hfs axes ($A_{\parallel}$), 109° apart from each other; in the coordinate system of Fig. 3, one is along $[11\bar{1}]$ and the other along $[1\bar{1}1]$. This is confirmed by the fact that the $P4$ hfs satellites split in two as the magnetic field moves from ⟨110⟩ toward the ⟨111⟩ axis in the {110} plane

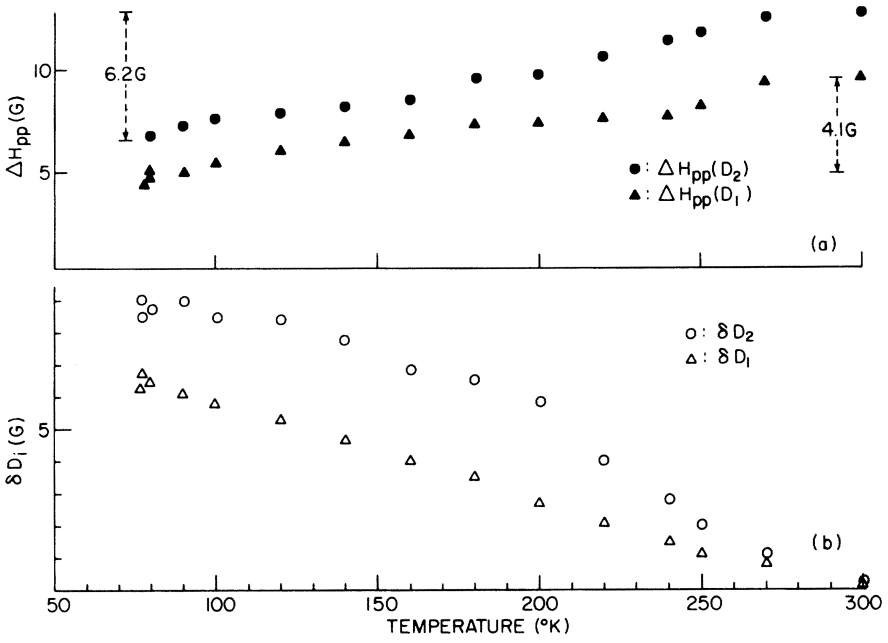

FIG. 9. Temperature dependence in the $A14$ [V_2+O] spectrum: (a) the linewidth (ΔH_{pp}) when $\vec{H}_0$ is perpendicular to the D_1 axis (▲) and $\vec{H}_0$ is parallel to the D_2 axis (●); (b) the D-value shift [$\delta D = H(T) - H$ (300 °K)] when $\vec{H}_0$ is parallel to the D_1 axis (△) and $\vec{H}_0$ is parallel to the D_2 axis (○), where $H(T)$ denotes the splitting between a pair of the fine structure at a given temperature T. ($\Delta H_{pp} = 6.2$ G and $\delta D = 0$, regardless of temperature, when $\vec{H}_0$ is parallel to the D_3 axis.)

and converge back to one at ⟨100⟩ as shown in Fig. 8(b). The $P4$ spectrum reveals another set of the ^{29}Si hyperfine structure with the hfs splittings ~3.0 G and the intensity ratio 26% (~10–11 equivalent sites); this hfs separation is too small to resolve its anisotropy.

C. Temperature dependence of Si-A14

The temperature dependence of the $A14$ spectrum was studied in the temperature range 77–300 °K; no variation in either the g or A tensor was observed outside the error range, but the magnitude of the zero-field splitting and the peak-to-peak linewidth of the fine-structure lines change with temperature. This is shown in Fig. 9, where $\Delta H_{pp}(D_i)$ is the peak-to-peak width of the line for $\vec{H}_0$ along the D_i axis and $\delta D_i = H_i(T) - H_i(300\,^{\circ}\mathrm{K})$, where H_i ($i = 1, 2$) is the value (in gauss) of the separation between the fine-structure pair corresponding to the electronic transitions, ($m = 0 \rightarrow m = +1$) and ($m = -1 \rightarrow m = 0$), when the external magnetic field is along the D_i principal axis. The D values along the D_1 and D_2 axis increase with decreasing temperature but the amount of the increase is anisotropic; $\delta D_1 = 6.5$ G, $\delta D_2 = 9.0$ G, at 77 °K, and the ratio $\delta D_1 : \delta D_2 = 2:3$ holds nearly constant throughout the temperature range we studied. The linewidth is linearly proportional to temperature [Fig. 9(a)]; $\Delta H_{pp}(D_1)$ broadens by 4.1 G in the range 77–300 °K, while $\Delta H_{pp}(D_2)$ increases by 6.2 G. The ratio $\Delta H_{pp}(D_1) : \Delta H_{pp}(D_2)$ is again 2:3, in agreement with that of δD_i's. When the magnetic field is parallel to the D_3 axis, no change was observed in the D_3 value and its linewidth; $\Delta H_{pp}(D_3) = 6.2$ G and $\delta D_3 = 0$ throughout the temperature range. It is clear therefore that the D-tensor variation with temperature is closely correlated with the change in ΔH_{pp}.

The variation of an EPR parameter (D) with temperature can be divided into two parts[39]; i.e.,

$$\left(\frac{\partial D}{\partial T}\right)_P = \left(\frac{\partial D}{\partial T}\right)_V - \alpha B \left(\frac{\partial D}{\partial P}\right)_T , \qquad (2)$$

where $\alpha = (\partial V/\partial T)_P$ is the local volume expansion coefficient and $B = (\partial P/\partial V)_T$ the bulk modulus. The first term represents the "explicit" temperature dependence (or that due to lattice vibration) and the second term is the "implicit" term (or that due to a thermal expansion). Since δD_1 through thermal expansion is probably less than 0.3 G [which is estimated from our uniaxial stress result, that $(\partial D_1/\partial P)_T / D_1 < -4 \times 10^{-5}$ atm^{-1}], the implicit contribution should be much less than 5% of the total D-tensor variation in the $A14$ spectrum. The anisotropic effect in δD_i and ΔH_{pp} strongly suggests that the dominant effect is due to the explicit contribution from lattice vibration, but a detailed theoretical treatment is obviously required to understand this unusual temperature effect.

IV. DISCUSSION

A. Defect models

We will construct a microscopic defect model for the oxygen-dependent spin-1 centers ($A14$, $A15$, $P2$, $P4$, $P5$). (In all cases we consider the model with a metastable triplet state.) Our argument will be mostly based on our results on the coupling tensors ($\overleftrightarrow{g}$, $\overleftrightarrow{A}$, $\overleftrightarrow{D}$) and the annealing be-

havior. Further confirmation of the models from the stress alignment data will be presented in Sec. V.

I. Si-*A14* $[V_2+O]$

Figure 10(a) shows the assumed defect model for the *A*14 spectrum; it consists of a divacancy and a nearly substitutional oxygen which is trapped near a vacancy site forming the Si-O-Si bond structure (as in the $[V+O]^-$ center[23]). Its qualitative electronic structure is shown in Fig. 10(b). Here, we have assumed: (i) that the bond strength of the Si-O-Si bond is stronger than that of the Si-Si bond, based on the fact that the bond dissociation energy[40] of the diatomic molecule is 8.17 eV/molecule for O-Si, 5.17 eV/molecule for O–O, and 3.30 eV/molecule for Si-Si (these values may be somewhat different in the Si lattice); (ii) that the oxygen atom interacts only with its nearest neighbors since the average Hartree-Fock radii[41] of the outer valence electrons are $\langle r\rangle_{3p}=1.46$ Å for Si, $\langle r\rangle_{2p}=0.65$ Å for O; and (iii) that the six Si dangling bonds surrounding the divacancy are made of the tetrahedral sp^3 hybrid orbitals (ϕ_a, ϕ_b, ϕ_c, ϕ_d, ϕ_e, ϕ_f). The orthonormal hybrid orbitals on the oxygen (O) atom are constructed by taking into account only the Si(e)-O-Si(f) bond so that the two orbitals are respectively directed toward the Si(e) and Si(f) atoms; i.e.,

$$\psi_1=(1/\sqrt{2})[(2-\csc^2\tfrac{1}{2}\theta)^{1/2}S+(\cot\tfrac{1}{2}\theta)P_x-P_y]\,, \tag{3a}$$

$$\psi_2=(1/\sqrt{2})[(2-\csc^2\tfrac{1}{2}\theta)^{1/2}S+(\cot\tfrac{1}{2}\theta)P_x+P_y]\,, \tag{3b}$$

$$\psi_3=(\cot\tfrac{1}{2}\theta)S-(2-\csc^2\tfrac{1}{2}\theta)^{1/2}P_x\,, \tag{3c}$$

$$\psi_4=P_z\,, \tag{3d}$$

where θ is the angle between the bonds, Si(e)-O and O-Si(f) ($\theta=109°$ for the tetrahedral configuration), and the coordinate system is indicated in Fig. 10(a). Thus, the orbitals ψ_1 and ψ_2 overlap very strongly with the ϕ_e and ϕ_f, respectively, and weakly with the others. The figure shows bonding ($\Psi_b\sim\phi_a+\phi_d$) and antibonding ($\Psi_A\sim\phi_a-\phi_d$) combinations of the bonds at the end of the chain, with one electron in Ψ_A because of thermal excitation. In so doing, we presume that ϕ_a and ϕ_d are equivalent, even though ϕ_d is nearer the oxygen than ϕ_a. For this C_{1h} symmetry all these states have Γ_1 (or A' symmetry) and hence can interact via configuration interaction. A full theoretical treatment of this defect is beyond the scope of this paper; here we only discuss the qualitative features required by the data. First we will review briefly what has emerged by way of theoretical understanding of the nature of the states of these defects. Watkins and Messmer[42] have shown that the simple one-electron method provides a valid first-order treatment of such defects. As an example consider the divacancy. [See Fig. 10(a), which is the same as the divacancy model if oxy-

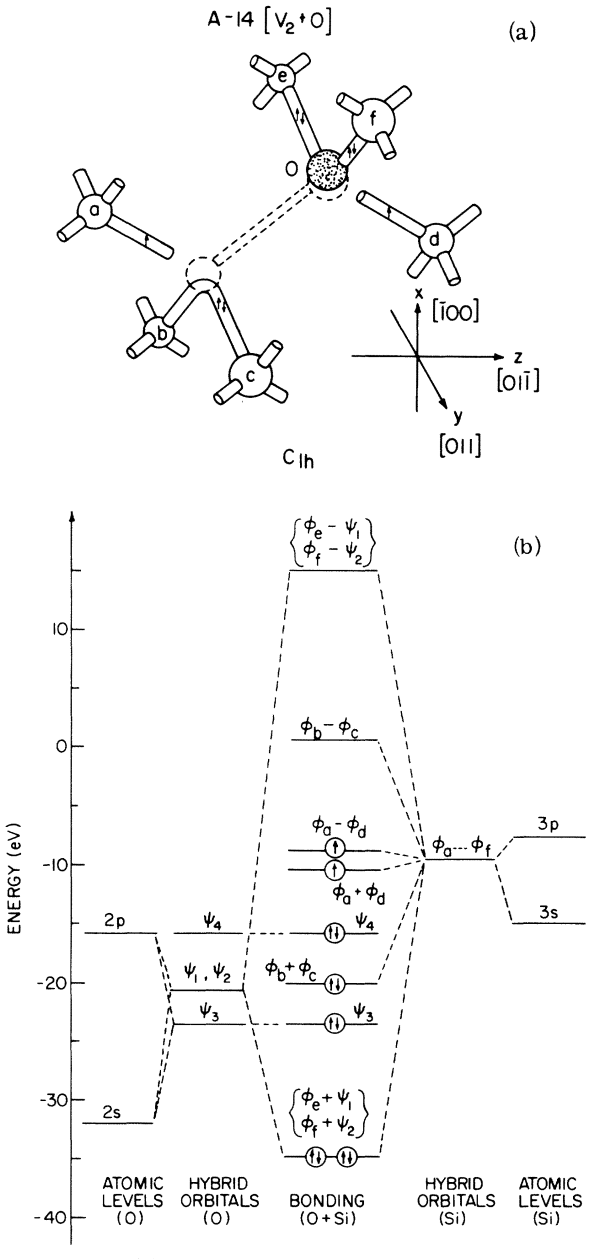

FIG. 10. (a) Atomic configuration of the *A*14-defect model $[V_2+O]$. (b) Schematic (see text) electronic structure of $[V_2+O]^0$; each atomic orbital is defined by its ionization potential and the energy levels for the hybrid orbitals are from their expectation values of the atomic Hamiltonian, e.g., $E(sp^3)=0.25E(3s)+0.75E(3p)$. The hybrid levels for oxygen are determined for the tetrahedral bonding structure ($\theta=109°$). The energy splitting between the bonding and antibonding orbitals of ϕ_a and ϕ_d is exaggerated in the figure to emphasize the splitting.

gen is removed.] In forming the "defect molecular" states the dominant interaction is a bonding distortion which permits pair-wise bonding of neighbors of the vacant sites, in this case atoms "*b* and *c*" and "*e* and *f*." That interaction leaves the orbitals at the end of the vacancy string (on atoms *a* and *d*) uncoupled. For the spin-$\frac{1}{2}$ (one-unpaired-electron) states which have been observed $[V_2]^{\pm}$, it suffices to consider the bonding (E_B) and antibonding (E_A) states formed from these states. $[V_2]^-$ is the state with an unpaired electron at the antibonding level and $[V_2]^+$ with an electron at the bonding state. It follows then that the ground state of the neutral charge state of $[V_2+\mathrm{O}]$ is a singlet. The fact[43] that the *P*3 and *P*4 spectra are absent at 4.2 °K seems to suggest that the spin-1 centers may arise from a metastable excited state through thermal excitation.[3] (A detailed study on the temperature dependence is required to prove this point.)

This model, in fact, satisfies our experimental results: the symmetry of *g* and *D* tensors is consistent with the defect symmetry; the bond axes of ϕ_a and ϕ_d are parallel to a ⟨111⟩, as observed in the ^{29}Si hyperfine structure; the *g* shifts ($\Delta g_{\parallel} = -0.0001$, $\Delta g_{\perp} = 0.0065$) are what we expected from the "parallel pair bond."[4] Because of the strong Si-O-Si bond, the motional effect between the Jahn-Teller distortions, as observed in the $[V_2]^{\pm}$ centers[15] would not occur in this model, consistent with the temperature dependence of the linewidth.

2. Si-*P2* $[V_2+\mathrm{O}_2]$

The defect model of the *P*2 spectrum is shown in Fig. 11(a). The two oxygen impurities (O′, O″) are trapped at the two vacancy sites, respectively, giving two Si-O-Si structures. Since the defect has the C_{2h} symmetry, $\psi_3(\mathrm{O}')$ and $\psi_4(\mathrm{O}')$ are allowed to interact, respectively, with $\psi_3(\mathrm{O}'')$ and $\psi_4(\mathrm{O}'')$, so that the two oxygen atoms are double bonded by two π-type bonds. However, we expect the total bond strength between two oxygens to be weak compared with the Si-O-Si σ bonding and the two oxygens would not form an oxygen molecule. This model not only satisfies the previous results on the *g* and *D* tensors but is consistent with our new result on the ^{29}Si hyperfine structure which requires two dangling bonds with the same ⟨111⟩ axis. The symbols $\psi_4 \oplus \psi_4$ and $\psi_4 \ominus \psi_4$ denote the symmetric and antisymmetric combinations of the p_z functions, e.g., the symmetric is $[p_z(\mathrm{O}'') - p_z(\mathrm{O}')]$.

3. Si-*P4* $[V_3+\mathrm{O}]$

Figure 11(b) is the model for the *P*4 spectrum, where one oxygen is trapped at the end of a three vacancy chain along a ⟨110⟩ axis. This model is the same as the one Brower[19] suggested implicitly. The symmetry is reduced to C_{1h} by the presence of an oxygen, as indicated in the symmetry of both the *g* and *D* tensors. We suggest that such a distortion does not severely influence the resonant wave function because the ionic size of oxygen is very small. Thus the wave function localized at the *d* site appears to be equivalent to that at the *a* site, with the difference between them within the error range. Two dangling bonds (ϕ_a, ϕ_d) are 109° apart from each other, which is consistent with experiment as we will discuss later in Sec. IV C. The asymmetric two oxygen model which also satisfies the symmetry can be ruled out since the defect concentration of $[V_3+\mathrm{O}]$ is comparable to that of $[V_2+\mathrm{O}]$.

4. Si-*P5* $[V_3+\mathrm{O}_2]$

The defect model for the *P*5 spectrum is shown in Fig. 11(c). Two oxygens are trapped at both ends of a trivacancy chain, giving rise to the C_{2v} symmetry as we observed in the *g* and *D* tensors. Although one oxygen at the middle of the trivacancy satisfies the symmetry requirement, this possibility is excluded by the fact that $[V_3+\mathrm{O}]$ is simultaneously present and the $[V_3+\mathrm{O}_2]$ appears only when $[V_2+\mathrm{O}_2]$ begins to disappear near 400 °C.

5. Si-*A15* $[V_3+\mathrm{O}_3]$

The defect model for *A*15 is shown in Fig. 11(d). The arguments concerning the bonding, symmetry and energy levels is essentially the same as for the $[V_3+\mathrm{O}_2]$ center, which also has C_{2v} symmetry.

B. Annealing kinetics

It is well known in silicon that the oxygen-associated vacancy defect is much more stable than the intrinsic vacancy defect (e.g., the $[V+\mathrm{O}]^-$ center anneals at 350 °C, whereas $[V]^{\pm}$ centers disappear below − 200 °C). But we see here that $[V_2]^{\pm}$ and the $[V_2+\mathrm{O}]$ anneal at about the same temperature (350 °C). This suggests that $[V_2+\mathrm{O}]$ might not dissociate into smaller point defects at that temperature, but acts as a sink to trap other point defects. When $[V_2+\mathrm{O}]$ acquires an extra vacancy, which is presumably created by the dissociation of $[V_2]$, it converts to $[V_3+\mathrm{O}]$. When $[V_2+\mathrm{O}]$ traps an additional oxygen released by $[V+\mathrm{O}]$, (which also anneals in this temperature range), it becomes $[V_2+\mathrm{O}_2]$. Because of the smaller intensity of $[V_2+\mathrm{O}_2]$ (see Fig. 5), most of the oxygens released by $[V+\mathrm{O}]$ at 350 °C return to the normal interstitial site of oxygen (the bond-center position) and only a small portion of them participate in the defect transition. By 400 °C, $[V_2+\mathrm{O}_2]$ transforms to $[V_3+\mathrm{O}_2]$ or $[V_3+\mathrm{O}_3]$ by trapping a vacancy or a vacancy plus oxygen. The mechanism of the loss of the trivacancy complexes is not clear.

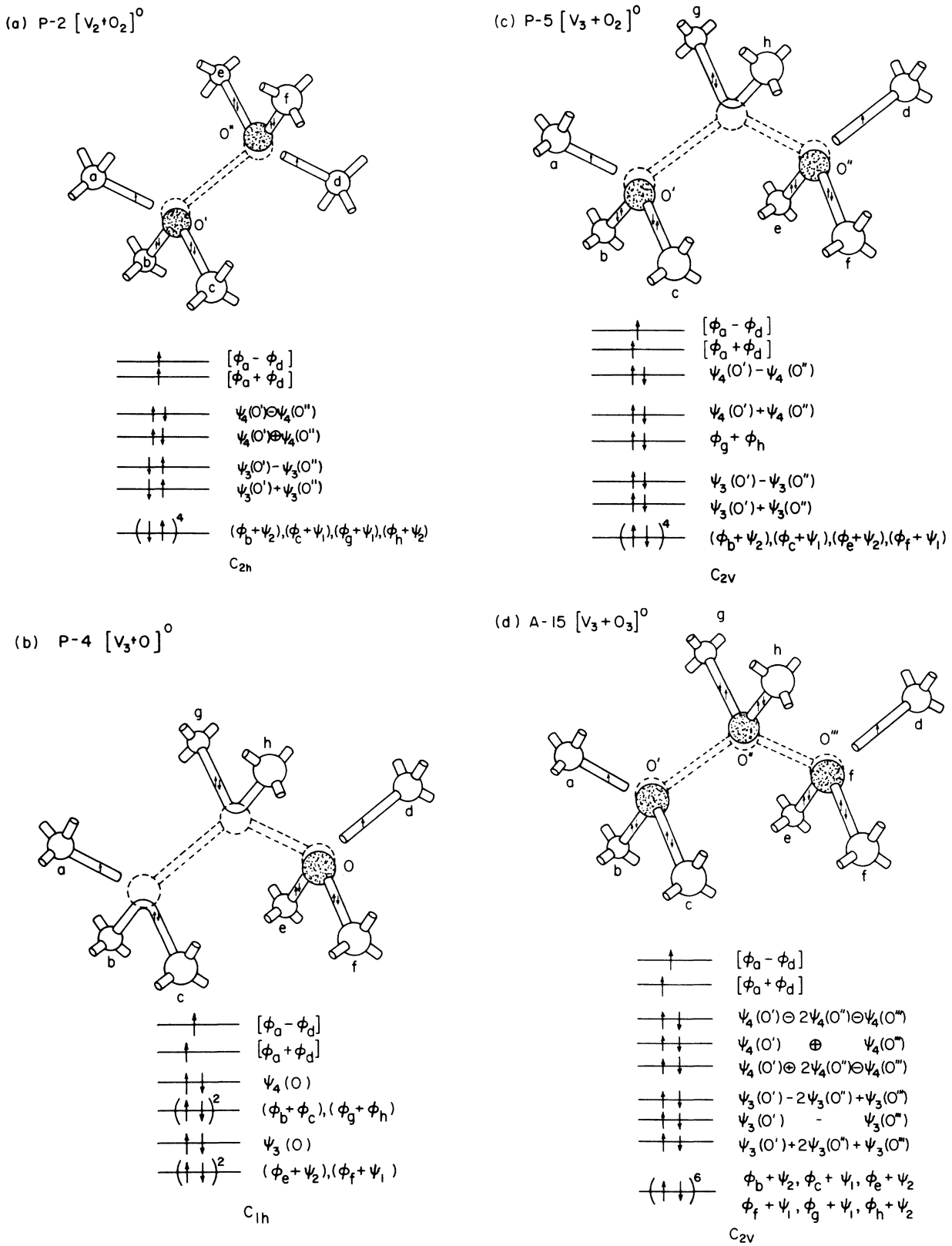

FIG. 11. Defect models and schematic electron configuration: (a) $[V_2+O_2]$ for the $P2$ spectrum; (b) $[V_3+O]$ for the $P4$ spectrum; (c) $[V_3+O_2]$ of the $P5$ spectrum; (d) $[V_3+O_3]$ of the $A15$ spectrum. The symbols $\psi_4\oplus\psi_4$ and $\psi_4\ominus\psi_4$ denote the symmetric and antisymmetric combinations of the p_z functions, e.g., $\Psi_4(O')\oplus\psi_4(O'')$ is essentially $p_z(O'')-P_z(O')$.

TABLE II. Hyperfine parameters and wave-function coefficients.

Spectrum model	aj (10^{-4} cm^{-1})	b_j (10^{-4} cm^{-1})	α_j^2	β_j^2	η_j^2	$\sum_j^N \eta_j^2$	Number of sites (N)
Si-A14 [V_2 + O]	50.9	9.30	0.12	0.88	0.31	0.62	2
Si-P2 [V_2 + O_2]	46.7	9.70	0.11	0.89	0.32	0.64	2
Si-P4 [V_3 + O]	52.2	6.73	0.16	0.84	0.24	0.48	2
	5.6	0.	1.0	0.	0.004	0.05	~12

More detailed studies are required to establish the actual energetics of all these processes.

C. Hyperfine interaction

The Hamiltonian for the hyperfine interaction is

$$\mathcal{H} = [(\vec{\mu}_e \cdot \vec{\mu}_N)/r^3 - 3(\vec{\mu}_e \cdot \vec{r})(\vec{r} \cdot \vec{\mu}_N)/r^5] - \tfrac{8}{3}\pi \vec{\mu}_N \cdot \vec{\mu}_e \delta(\vec{r}) - |\vec{\mu}_e|(\vec{\mu}_N \cdot \vec{L})/r^3 , \quad (4)$$

where the first terms are the magnetic dipole-dipole interaction between the electronic magnetic moment ($\vec{\mu}_e = g_0 \mu_B \vec{S}$) and the nuclear moment ($\vec{\mu}_N = g_N \mu_N \vec{I}$), the second term is the Fermi contact interaction and the third one the orbital interaction of the electron with the nuclear magnetic moment. The orbital term does not contribute to the hyperfine interaction in the zero-order approximation, since we know from the g tensor that the orbital angular momentum is very much quenched; however, it does appear in second order, predominantly, through the spin-orbit interaction. If the g shift is significant, the second-order contribution cannot be ignored. Thus, if we include the second-order perturbation of Eq. (4) via the spin-orbit interaction,[44] an axially symmetric A tensor for the jth nucleus can be described as follows:

$$A_{\parallel}^j = a_j + (2 - \tfrac{3}{2}\Delta g_{\perp}) b_j \quad (5a)$$

and

$$A_{\perp}^j = a_j - (1 - \tfrac{13}{4}\Delta g_{\perp}) b_j , \quad (5b)$$

where

$$a_j = \tfrac{8}{3}\pi g_0 g_N \mu_B \mu_N \alpha_j^2 \eta_j^2 |\phi_{3S}(0)|_j^2$$

and

$$b_j = \tfrac{2}{5} g_0 g_N \mu_B \mu_N \beta_j^2 \eta_j^2 \langle r_{3P}^{-3} \rangle_j .$$

We assumed here that (a) the resonant wave function is composed of hybrid orbitals on each end of the chain, i.e., $\Psi = \sum_j \eta_j (\alpha_j \phi_{3S}^j + \beta_j \phi_{3P}^j)$ (with $\alpha_j^2 + \beta_j^2 = 1$ and $\sum_j \eta_j^2 = 1$), and that (b) the g tensor is also axially symmetric.

Using $g_N = -1.1106$, $|\phi_{3s}(0)|^2 = 31.5 \times 10^{24}$ cm^{-3}, and $\langle r_{3p}^{-3} \rangle = 16.1 \times 10^{24}$ cm^{-3} for the ^{29}Si atom,[28] the parameters, α_j^2, β_j^2, and η_j^2, of the resonant wave function are estimated for the A14 [V_2+ O], P2 [V_2+ O_2], and P4 [V_3+ O] spectra and are given in Table II. Since the second order correction [the terms involving $\Delta g_{\perp}$ in Eq. (5)] are found to be less than 3% (e.g., the error in η_j^2 is only 0.025 for [V_2 + O]), our calculation is based on the zero-order alone. The resonant wave function of the A14 spectrum consists of the 12% s and 88% p wave function and only 31% of the total wave function is equally localized at each of two nuclear sites; the remaining 38% is presumably associated with orbitals on other neighboring atoms. The hfs structure of P4 accounts for only 53% of the wave function, even including the other resolved hyperfine interactions.

For all three complexes, the hybrid orbital has a strong p character. This is in fact one of the common features in the vacancy-associated defects in silicon.[4] From the anisotropy of the g and D tensors, the vacancies must contain a {110} symmetric plane whose normal is parallel to the g_2 (and D_2) axis. Whether there are odd or even number of vacancies along the ⟨110⟩ chain can be deduced from the axis of the hyperfine component ($A_{\parallel}$); both A14 [V_2+ O] and P2 [V_2+ O] spectra must involve even number of vacancies because the bond axis of the two dangling bonds are parallel; the P4 [V_3+ O] spectrum must contain an odd number of vacancies because the two bond axes are canted to each other by 109° in the same {110} plane.

Therefore, the hyperfine structure strongly support the assumption that the defects responsible for the A14, P2, and P4 spectra are indeed vacancies in the {110} plane trapped by impurity oxygen(s).

D. Electronic spin-spin interaction

As we have discussed in Sec. IV C the resonant wave function is mostly localized at two nuclear

sites. The two spins, each of which resides at a different atomic site, are interacting with each other, forming a spin triplet state. The interactions between a pair of spins have been reviewed elsewhere[45] in great detail. In all the spin-1 centers we mentioned above, all the experimental data are describable by a symmetric, traceless tensor $\overleftrightarrow{D}$.

Jung and Newell[3] argued that the fine structure of the $P3$ spectrum is mainly due to the magnetic dipole-dipole interaction,

$$D_{ij} = \tfrac{1}{2} g_0^2 \mu_B^2 \langle (\vec{S}_1 \cdot \vec{S}_2)/r^3 - 3(\vec{S}_1 \cdot \vec{r})(\vec{S}_2 \cdot \vec{r})/r^5 \rangle \ . \tag{6}$$

They estimated (erroneously[46]) that the distance between the two spins might be ~5.42 Å, i.e., the lattice constant. Thus, for the $P3$ spectrum, the experimental D values were about the values predicted by Eq. (6) for $[V_2]$. Brower[19,24] extended their argument to include other spin-1 centers using a correct estimate of the D values and proposed the defect models for $P2$, $P4$, and $P5$ similar to ours in Sec. IV A. Figure 12 shows the D_1 value with respect to the distance between two spins estimated from Eq. (6) for σ- and π-bonding orbitals. Also plotted are all the experimental D_1 values for the spin-1 centers in silicon, except $[V+\mathrm{Al}]$. The D values indicate a one vacancy distance for $[V+\mathrm{O}]$, a two vacancy distance for $[V_2+\mathrm{O}]$ and $[V_2+\mathrm{O}_2]$, a three vacancy length for $[V_3+\mathrm{O}]$, $[V_3+\mathrm{O}_2]$, and $[V_3+\mathrm{O}_3]$ and a four vacancy length for $[V_4]$. Detailed studies confirm that the SL-1 spectrum[24,25] arises from a triplet (excited) state of the well-known $[V+\mathrm{O}]$ center. Studies on the $P3$ spectrum also indicate that it is a {110} planar tetra-vacancy chain.[19,47]

Equation (6) satisfactorily accounts for $\overleftrightarrow{D}$ for all the centers, consistent with our defect models, except $[V+\mathrm{Al}]$ where a large D value ($D_1 = 0.2809$ cm^{-1}) was attributed to the spin-orbit interaction.[29] The spin-orbit interaction cannot be a major origin for the fine structure of all the oxygen-dependent spin-1 centers we are dealing with, because D_{ij} is not proportional to Δg_{ij} in the spin-1 centers in Table I. (This proportionality holds in $[V+\mathrm{Al}]$.)

Another possible origin could be the super-exchange interaction,[48] which might take place through an oxygen impurity in the oxygen-vacancy complexes. Moriya[49] showed that the symmetric part of the traceless D tensor is proportional to the square of Δg_{ij} [i.e., $D_{ij} \sim 2J(\Delta g_{ij}/g_{ij})^2$, where J is the isotropic super-exchange interaction]. Thus, the super-exchange contribution is too small to be the dominant source of D_{ij}. We note however that there is a systematic trend in the defects containing oxygen, i.e., the more oxygen, the larger the D tensor. We suggest that this latter small effect may be due to a super-exchange interaction.

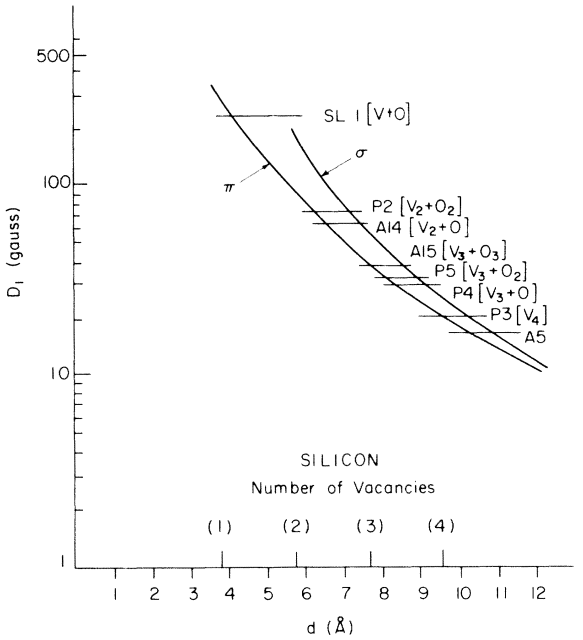

FIG. 12. Principal D values vs the separation between two interacting ions; the calculation is based on the point dipole model. The D_1 values of all the spin-1 centers (excluding only $G9$ $[V+\mathrm{Al}]$) in silicon are listed wtih a bar. The abscissa is also calibrated in number of vacancies between the two occupied end sites on a ⟨110⟩ chain of vacancies.

We argue this because the differences in the D tensors and the g shifts in sequences ($[V_2+\mathrm{O}]$, $[V_2+\mathrm{O}_2]$) and ($[V_3+\mathrm{O}]$, $[V_3+\mathrm{O}_2]$, $[V_3+\mathrm{O}_3]$) each show a "Δg_{ij}-vs-D_{ij}" relationship and yield a $J \sim 0.01$ eV in all cases.

V. STRESS EFFECTS

The response of the $A14$ $[V_2+\mathrm{O}]$, $P2$ $[V_2+\mathrm{O}_2]$, and $P4$ $[V_3+\mathrm{O}]$ spectra to an ⟨110⟩ uniaxial stress at an elevated temperature provides additional important support for the defect models. Figure 13 shows typical data for the $P2$ and $P4$ spectra; (a) the actual spectra taken before the sample were stressed and (b) the same spectra after the sample were cooled down to room temperature from 185 °C under the ⟨110⟩ stress (2450 kg/cm^2). Each fine-structure line is indicated in terms of its defect orientation (see Fig. 3). The defect ad is the one with its g_2 axis (Si-O-Si bonding direction) parallel to the ⟨110⟩ stress direction and bc is the defect whose g_2 axis is perpendicular to the stress axis. Watkins and Corbett[15] observed that the divacancy is preferentially aligned under a ⟨110⟩ compression in favor of the defect whose orientation is such that the axis joining the pair-bonding silicon atoms (g_2 axis) is parallel to the stress. The compression pushes the pair-bonding atoms [for instance, the atoms b and c in Fig. 10(a)] closer

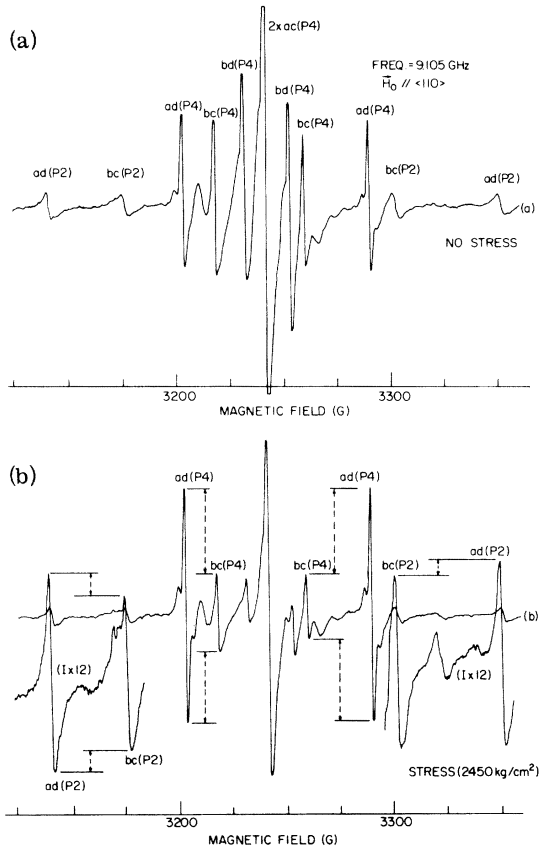

FIG. 13. Anisotropic stress alignment of differently oriented equivalent defects in the $P2$ and $P4$ spectra; (a) before an external stress was applied, and (b) after the sample was cooled down to room temperature from 185 °C under a ⟨110⟩ axial stress. A considerable change in the intensity of the *ad* and *bc* lines is indicated by a dashed line.

together so as to lower their energy. We observe the same effect here in $[V_2+O_2]$ and $[V_3+O]$; i.e., under ⟨110⟩ compression, the number of defects at the *ad* site is increased, whereas the number at the *bc* site is decreased ($N_{ad}>N_{ab}>N_{bd}>N_{bc}$). A similar experiment was also performed for $[V_2+O]$ applying the ⟨110⟩ stress (2100 kg/cm²) at 190 °C. The $[V_2+O]$ center is aligned in favor of the defect site whose g_2 axis is parallel to the stress, as in the case of $[V_2+O_2]$ and $[V_3+O]$.

The degree of alignment, defined as

$$n_\perp/n_\parallel = (N_{ad}+N_{ab}+N_{ac})/(N_{bc}+N_{ba}+N_{bd}) , \tag{7}$$

is estimated from the alignment data and the results are presented in the last column of Table III.

We analyzed previously[47] the quenched-in alignment in terms of the piezospectroscopic tensor $(\overleftrightarrow{B})$. For the C_{1h}-symmetric defect, the defect concentration of each defect type (N_{ad}, N_{ac}, N_{bc}, N_{bd}) is proportional to the Boltzmann factor at a given temperature (T). Thus, the relative concentration in the deformed crystal can be written

$$N_{ad}/N_{bc} = \exp(-T_\alpha/T) , \tag{8a}$$

$$N_{ad}/N_{ac} = \exp(-T_\beta/T) , \tag{8b}$$

$$N_{ac}/N_{bd} = \exp(-T_\gamma/T) , \tag{8c}$$

with

$$kT_\alpha = -\tfrac{1}{2}pS_{44}(B_2-B_1) ,$$

$$kT_\beta = -\tfrac{1}{4}p[(S_{11}-S_{12}-S_{44})B_1+(S_{11}-S_{12}+S_{44})B_2 - 2(S_{11}-S_{12})B_3-\sqrt{2}S_{44}B_4] ,$$

$$kT_\gamma = -(p/\sqrt{2})S_{44}B_4 ,$$

where p is the external stress, k is the Boltzmann constant, and $\overleftrightarrow{S}$ is the elasticity tensor of the host lattice ($S_{11}=7.68\times10^{-13}$ cm²/dyn, $S_{12}=-2.14\times10^{-13}$ cm²/dyn, $S_{44}=12.56\times10^{-13}$ cm²/dyn). The parameters, B_1, B_2, B_3 are the change in the defect energy due to the stress along the $[01\bar{1}]$, $[011]$, $[\bar{1}00]$ axes, respectively [see Fig. 10(a)]. B_4 is the defect energy change in the $(01\bar{1})$ plane by a shear stress. Using Eqs. (8) the piezospectroscopic parameters for the $A14$, $P2$, $P4$ spectra are estimated as given in Table III; B_4 can be calculated directly from Eq. (8c), but estimation of B_1, B_2, and B_3 requires an assumption [either $\mathrm{tr}(\overleftrightarrow{B})=0$ or $B_3=0$], because the hydro-

TABLE III. Parameters of piezospectroscopic tensor under the ⟨110⟩ uniaxial compression [in eV/(unit strain)]. The values in parentheses are calculated on the assumption $B_3=0$.

Spectrum model	Stress (kg/cm²)	Temp. (°C)	T_α (°K)	T_β (°K)	T_γ (°K)	B_1	B_2	B_3	B_4	$n_\perp/n_\parallel$
Si-$A14$ $[V_2+O]^\circ$	2100	190	−185.2	−5.12	−172.6	−5.76 (−4.72)	6.59 (7.63)	0.83 (0)	8.14	1.50
Si-$P2$ $[V_2+O_2]^\circ$	2450	185	−232.1	−46.4	−146.2	−6.07 (−4.63)	7.21 (8.65)	−1.14 (0)	5.91	1.46
Si-$P4$ $[V_3+O]^\circ$	2450	185	−396.2	−368.4	−378.2	−1.06 (25.0)	21.6 (47.2)	−20.5 (0)	15.3	2.33

static pressure data are not available for any defect in silicon (for details, see Ref. 49).

$n_\perp/n_\parallel > 1.0$ implies that more "bent-pair bonds" [e.g., b-c bond in Fig. 10(a)] are in the direction along the g_2 axis than along other principal axes which is also the case for the {110} planar vacancy chain defects.[47] This is actually consistent with our defect models for the $A14$, $P2$, and $P4$ spectra. This argument is further supported by a large positive value in the B_2 parameter and a small negative value in the B_1 parameter in these spectra. In $[V_2+O]$ (Fig. 10), we see that one Si-Si bonding orbital ($\phi_b+\phi_c$) and one Si-O-Si orbital ($\phi_e+\psi_1$, $\phi_f+\psi_2$) shift their energy levels lower when the pairs of atoms, b and c, e and f are forced closer together by the stress along the [011] axis. Thus, the B_2 value is expected to be positive and the largest of the four parameters, consistent with the results in Table III. When the stress is along the $[01\bar{1}]$ axis (the B_1 direction), the antibonding orbital ($\phi_a-\phi_d$) moves up, resulting in a negative B_1 value (a small B_1 is due to a weak coupling between the ϕ_a and ϕ_d orbitals). We anticipate a similar result in $[V_2+O_2]$ [Fig. 11(a)], since the energy change in the Si-O-Si bonding orbital is almost the same as that in the Si-Si bonding orbital as observed in[32] $[V+O]$ [$B_{\text{Si-Si}}=16$ eV/(unit strain), $B_{\text{Si-O-Si}}=17.2$ eV/(unit strain)]. The B_1 value should be a small negative value too, because the antibonding orbital ($\phi_a-\phi_d$) goes up as the two atoms a and d come closer together. In $[V_3+O]$ [Fig. 11(b)], we expect a positive B_2 value which is larger than that for $[V_2+O]$ and $[V_2+O_2]$ (since it contains two "Si-Si" and one "Si-O-Si" bond structures) and a small negative B_1 for the same reason as in $[V_2+O]$ and $[V_2+O_2]$. We find a considerably larger B_3 and B_4, which indicates that the actual defect is significantly distorted from the frozen lattice model. This is also what we expect from the g and D tensors of $[V_3+O]$.

Therefore, our stress results agree fairly well with our expectation from the defect models, and we will take these results as strong confirmation for our defect models.

VI. SUMMARY AND CONCLUSION

Three new EPR spectra, Si-$A14$, -$A15$, and -$A16$ are reported in this paper and the five spin-1 centers, Si-$A14$, -$A15$, -$P2$, -$P4$, and -$P5$ are studied in detail. They are all found to be due to various oxygen-associated defects produced by electron radiation. Although the two spectra ($P2$ and $P4$) were previously seen in the neutron- and in heavy-ion-bombarded silicon, this is the first time that these oxygen-dependent spin-1 centers are observed in electron-irradiated silicon.

A reasonable defect model is established for the oxygen-dependent spin-1 centers; the $A14$ spectrum (which anneals at 350 °C) is attributed to the one oxygen + divacancy complex $[V_2+O]^0$, the $P2$ spectrum to the two oxygen + divacancy complex $[V_2+O_2]^0$, the $P4$ spectrum to the one oxygen + trivacancy complex $[V_3+O]^\circ$, $P5$ to the two oxygen + trivacancy complex $[V_3+O_2]^0$, and the $A15$ to the three oxygen + trivacancy complex $[V_3+O_3]^0$. These defect models satisfy our EPR data: the symmetry of g and D tensors is consistent with that of the defect model; two broken bond axes (ϕ_a and ϕ_d) are parallel to the hyperfine axis of the $A_\parallel$ component; the magnitude of D_{ij} provides the reasonable number of vacancies along a ⟨110⟩ chain. The temperature dependence and quenched-in stress alignment provide additional supporting evidence.

Based on the identification of those oxygen-associated defects and their annealing behavior, we conclude that the stability of a defect in silicon is related to the number of oxygen atoms being trapped in the {110} planar multivacancy chain and that the oxygen-multivacancy complex plays an important role as a sink to trap other point defects such as a vacancy or an impurity.

ACKNOWLEDGMENTS

We wish to express our appreciation to our colleagues, Dr. L. J. Cheng, Dr. J. Rogers, and Dr. C. Weigel for helpful conversations and T. Bilash for the sample preparation.

---

*Work supported in part by the Office of Naval Research under Contract No. N00014-70-C-0296.

[1]G. D. Watkins, in *Radiation Damage in Semiconductors*, edited by P. Baruch (Dunod, Paris, 1965), p. 97.

[2]J. W. Corbett, *Electron Radiation Damage in Semiconductors and Metals* (Academic, New York, 1966), p. 59.

[3]W. Jung and G. S. Newell, Phys. Rev. 132, 648 (1963).

[4]Y. H. Lee and J. W. Corbett, Phys. Rev. B 8, 2810 (1973).

[5]M. Nisenoff and H. Y. Fan, Phys. Rev. 128, 1605 (1962).

[6]D. F. Daly and H. E. Noffke, in *Radiation Effects in Semiconductors*, edited by J. W. Corbett and G. D. Watkins (Gordon and Breach, New York, 1971), p. 179.

[7]We follow the standard nomenclature (Ref. 1) to label the spectra; Si-$A14$ means the 14th spectrum in silicon observed at Albany, etc. Since we are only concerned with silicon in this paper we will omit the Si prefix.

[8]G. D. Watkins, J. Phys. Soc. Jpn. 18, 22 (1963).

[9]G. D. Watkins, in *Radiation Effects on Semiconductor Components*, edited by F. Cambou (Journees d'Electronique, Toulouse, 1967), Vol. I, paper A1.

[10]G. D. Watkins, in *Radiation Effects in Semiconductors*, edited by F. L. Vook (Plenum, New York, 1968), p. 67.

[11]G. D. Watkins, Trans. IEEE NS-16, 13 (1969).

[12]G. D. Watkins, in *Radiation Effects in Semiconductors*, edited by J. W. Corbett and G. D. Watkins (Gordon and Breach, New York, 1971), p. 301.
[13]G. D. Watkins and J. W. Corbett, Discuss. Faraday Soc. 31, 86 (1961).
[14]J. W. Corbett and G. D. Watkins, Phys. Rev. Lett. 7, 314 (1961).
[15]G. D. Watkins and J. W. Corbett, Phys. Rev. 138, A543 (1965).
[16]J. W. Corbett and G. D. Watkins, Phys. Rev. 138, A555 (1965).
[17]Y. H. Lee, Y. M. Kim and J. W. Corbett, Radiat. Eff. 15, 77 (1972).
[18]Y. H. Lee and J. W. Corbett (unpublished).
[19]K. L. Brower, Radiat. Eff. 8, 213 (1971).
[20]G. Bemski, J. Appl. Phys. 30, 1195 (1959).
[21]G. D. Watkins, J. W. Corbett, and R. M. Walker, J. Appl. Phys. 30, 1198 (1959).
[22]G. D. Watkins and J. W. Corbett, Phys. Rev. 121, 1001 (1961).
[23]J. W. Corbett, G. D. Watkins, R. M. Chrenko, and R. S. McDonald, Phys. Rev. 121, 1015 (1961).
[24]K. L. Brower, Phys. Rev. B 4, 1968 (1971).
[25]K. L. Brower, Phys. Rev. B 5, 4274 (1972).
[26]G. D. Watkins [in *Lattice Defects in Semiconductors*, 1974 (Institute of Physics, London, 1975), p. 1] has reported "metastable" states of the (vacancy + oxygen) pair.
[27]Present paper.
[28]G. D. Watkins and J. W. Corbett, Phys. Rev. 134, 1359 (1964).
[29]G. D. Watkins, Phys. Rev. 155, 802 (1967).
[30]E. L. Elkin and G. D. Watkins, Phys. Rev. 174, 881 (1968).
[31]A. R. Bean, R. C. Newman, and R. S. Smith, J. Phys. Chem. Solids 31, 739 (1969).
[32]A. R. Bean and R. C. Newman, Solid State Commun. 8, 175 (1970).
[33]R. C. Newman and R. S. Smith, J. Phys. Chem. Solids 30, 1493 (1969).
[34]A. Brelot and J. Charlemagne, Radiat. Eff. 9, 65 (1971).
[35]A. Brelot, in *Radiation Damage and Defects in Semiconductors* (Institute of Physics, London, 1973), p. 191.
[36]K. L. Brower, F. L. Vook, and J. A. Borders, Appl. Phys. Lett. 15, 208 (1969).
[37]H. Luetgemeier and K. Schnitzke, Phys. Lett. A 25, 232 (1967).
[38]B. R. Gossick, J. Appl. Phys. 30, 1214 (1959).
[39]W. M. Walsh, Jr., J. Jeener, and N. Bloembergen, Phys. Rev. 139, 1338 (1965).
[40]*Handbook of Chemistry and Physics*, 52nd ed. (Chemical Rubber, Cleveland, 1971), p. F-177.
[41]C. F. Fischer, At. Data 4, 301 (1972).
[42]G. D. Watkins and R. P. Messmer, Phys. Rev. Lett. 32, 1244 (1974).
[43]W. Jung, Ph.D. thesis (Purdue University, 1963) (unpublished).
[44]A. N. Jette, Phys. Rev. 184, 604 (1969).
[45]J. Owen and E. A. Harris, in *Electron Paramagnetic Resonance*, edited by S. Geschwind (Plenum, New York, 1972), Chap. 6.
[46]Jung and Newell (Ref. 3) missed a factor of $\frac{1}{2}$ in their equation for the dipole-dipole interaction, which caused them to underestimate the distance between two interacting ions; the D value of $P3$ corresponds to 4 vacancy distance along $\langle 110 \rangle$.
[47]Y. H. Lee and J. W. Corbett, Phys. Rev. B 9, 4351 (1974).
[48]P. W. Anderson, in *Solid State Physics*, edited by F. Seitz and D. Turnbull (Academic, New York, 1963), Vol. 14, p. 99.
[49]T. Moriya, Phys. Rev. 120, 91 (1960).